First-Principles Modeling in Heterogeneous Electrocatalysis

Dominic R. Alfonso, [a] DeNyago Tafen, and Douglas Kauffmann

[1] *National Energy Technology Laboratory, U. S. Department of Energy, Pittsburgh, Pennsylvania 15236, USA*

The catalytic reduction of NO by CO on Rh(111) surface was extensively investigated by computational methods. Periodic density functional theory calculations were performed to elucidate the reaction mechanisms and possible products. The reaction energetics of all relevant elementary steps such as NO/CO adsorption, NO/CO dissociation, N_2 desorption, CO oxidation and CO_2 desorption were determined. The results show that the reduction process starts with NO dissociation as the corresponding CO dissociation is unlikely due to high energy barrier. The analysis also incorporates N_2 production occurring through classical surface N recombination step and via N_2O intermediate species from NO + N association process. The alternative pathway the proceeds through NO dimer formation is predicted to be difficult to achieve. Microkinetic modeling was carried out on the basis of these first principles data to predict the product distribution as a function of temperature. In addition to N_2 and CO_2, we provide theoretical confirmation that N_2O is also a major product. Our simulations are consistent with experimental results and can explain the formation of N_2O as a natural consequence of the reaction mechanism proposed.

[a] Electronic mail: alfonso@netl.doe.gov

I. INTRODUCTION

Electrochemical fuel generation whose basic principle is to catalytically produce valuable chemical compounds from inert reactants under mild conditions is predicted to become an important component of future energy infrastructures.[1-4] The electrode potential, adsorbates, catalyst structure and solution in the electrode/electrolyte interface lie at the heart of the electrochemical process. Experimental measurements are the usual path to characterize the interface as it is capable to provide observable characteristics such as surface tension, work function, interfacial capacitance.[5] However, experiments are limited to measurements of macroscopic equilibrium observables as virtually no instruments exist to elucidate the atomic level details of electrochemistry during operation. The lack of such probes makes it difficult to establish atomic scale interpretation of experimental data crucial for catalyst selection, design and application. Computations are usually performed using mean field equations such as Gouy-Chapman theory which assumes that the ions in the electrical double layer are point charges that interact only through Coulomb interactions.[6] However, these mesoscopic models are not generally transferable as they rely on system parameters fitted to experimental data. For these reasons, atomic level insights on cell electrochemistry remain elusive for these techniques, at least to date.

Aided by the concurrent advances in *ab initio* technique, computer hardware and numerical analysis over the last few decades, first principles modeling has made significant inroads into the simulation of electrochemical reactions catalyzed by solid surfaces.[7] It has become a valuable complementary tool to experiments at it provides molecular level description the bond breaking and forming on the catalyst coupled with

electron and ion transfer from one reactant to another allowing deconvolution of the plethora of process atomic processes at work. Recent advances have allowed the efficient accounting of the influences of the solvent on the catalyst interfacial properties.[8] Modeling the full details of the electrochemical phenomena has also become increasing accurate due to the development of quantum theory that explicitly includes the electrochemical potential.[9] Aside from hard to measure geometric structures and electronic properties, the output from the simulation includes reaction pathways and free energy profile. Indeed, elucidation of the otherwise ambiguous potentials from voltammetry and how they relate to atomic processes at the electrochemical interface can now be achieved from theory-experiment interplay.

In this account, we provided an overview of key concepts that enter into the theoretical modelling of electrochemistry. We first discussed the so-called zeroth-energy level protocol based on the electrochemical free-energy correction introduced by Norskov and co-workers which was used in large majority of simulations of heterogeneous electrocatalysis.[10] In this approach, the influence of electrode voltage is included *a posteriori* to reaction energy differences that involve electron transfer with either a dielectric continuum or atomistic representation of the solvent. We reviewed our specific application of this technique to the study of electrocatalytic CO_2 reduction and water oxidation on metal based nanoclusters. In subsequent sections, we discussed recent efforts to improve on the aforementioned approach by explicit inclusion of the electrochemical potential into the first-principles calculations. [9]

II. Computational Hydrogen Electrode Approach

The computational hydrogen electrode (CHE) approach pioneered by Norskov and co-workers represents a very promising way to enable modeling of electrochemistry by quantitatively incorporating insights from first-principles calculations.[10] The inclusion of quantum mechanical data imparts predictive capability and eliminates the need to make drastic simplifying assumption in the model. At the core of this approach is a specified reaction mechanism and the evaluation of the free energy of the corresponding elementary steps, $\Delta G = \Delta H - T\Delta S$. The key gateway to introduce electronic structure information into the model is via the free energy of individual component, $G_i = H_i - TS_i$, in each of the elementary step. The enthalpy of component i :

$$H_i = E_{el} + E_{solv} + E_{zpe} + E_{thermal} + PV \quad (1)$$

consists of the sum of electronic energy (E_{el}), solvation energy (E_{solv}), zero-point vibrational energy (E_{zpe}), thermal energy ($E_{thermal}$), and the PV term. The electronic energy may be calculated by a very high level of direct wave-function based approaches such as post Hartree-Fock methods.[11] Such computations, however, have a cost that grows very rapidly with the number of electrons in the system. Density functional theory (DFT) which reformulates the Schrodinger equation in terms of three-dimensional electron density without drastically compromising accuracy provides a cost-effective alternative.[7] Vast majority of first-principles CHE calculations have been done in combination with the DFT method.

Solvent effects are important in electrochemistry. The E_{solv} term accounts for the interaction of the species with the solvent which can be evaluated either by inclusion of bilayer of water or thru implicit solvation model. A particular advantage of the latter approach is that it circumvents phase space sampling difficulties associated with explicit

solvation treatments. A homogeneous constant dielectric continuum is employed to model the solvent but nevertheless can reproduce significant solvation energies in most situations.[12] The zero point energy correction is defined as:

$$E_{zpe} = \frac{1}{2}\sum h\nu_i \tag{2}$$

and the thermal energy includes translational, rotational and vibrational contributions:

$$E_{trans} = \frac{3}{2}RT \tag{3}$$

$$E_{rot}(\text{nonlinear molecule}) = \frac{3}{2}RT \tag{4}$$

$$E_{rot}(\text{linear molecule}) = RT \tag{5}$$

and

$$E_{vib} = R\sum \frac{h\nu_i/k_B}{e^{h\nu_i/k_BT}-1} \tag{6}$$

where k_B, h and R are the Boltzmann, Planck and gas constants. The vibrational frequencies ν_i can be efficiently calculated via DFT using the harmonic oscillator approximation by diagonalization of the mass-weighted Hessian matrix in internal coordinates. The corresponding translational, rotational and vibrational contributions to the entropy S_i are:

$$S_{trans} = R\left(\ln\left(\frac{(2\pi mk_BT)^{3/2}}{h^3}\right)+\ln\left(\frac{k_BT}{P}\right)+\frac{5}{2}\right) \tag{7}$$

$$S_{rot}(\text{nonlinear molecule}) = R\left(\ln\left(\frac{8\pi^2\sqrt{8\pi^3 I_x I_y I_z}(k_BT)^{3/2}}{\sigma h^3}\right)+\frac{3}{2}\right) \tag{8}$$

$$S_{rot}(\text{linear molecule}) = R\left(\ln\left(\frac{8\pi^2 Ik_BT}{\sigma h^2}\right)+1\right) \tag{9}$$

and

$$S_{vib} = R\sum_i \left(\frac{h\nu_i / k_B T}{e^{h\nu_i / k_B T} - 1} - \ln(1 - e^{-h\nu_i / k_B T}) \right) \quad (10)$$

where m is the mass of the species, P is the pressure, I_x, I_y, I_z are the three principal moments of inertia for nonlinear molecule, I is the moment of inertia for the linear molecule and σ is the rotational symmetry number.

For the H_i of gaseous molecule, E_{solv} is neglected in Eq. 1 and PV is set to RT assuming ideal gas. The translational, rotational and vibrational contributions to the S_i are considered. Evaluation of the entropy for the gaseous species can also be alternatively done using the Shomate equation:

$$S_i = A\ln(t) + Bt + \frac{Ct^2}{2} + \frac{Dt^3}{3} - \frac{E}{2t^2} + G \quad (11)$$

where $t = T/100$. The corresponding parameters A, B, C, D, E and G tabulated in the NIST database.[13] For its solvated counterpart, E_{solv} is included, PV is neglected and the three contributions to the entropic term are retained. For the solvated adsorbed species, the PV term is also excluded. However, for the thermal energy and entropy terms, only the vibrational component is considered. Thus, the free energy for the adsorbate is:

$G_{ads} = E_{el} + E_{solv} + E_{zpe} + E_{vib} - TS_{vib}$.

Within the CHE method, the influence of applied bias U in an electrochemical step is included by setting the total energy of the electron in the electrode to $-qU$ where q is the fundamental charge. Thus, the free energy of each step will vary with U according to:

$$\Delta G(U) = \Delta G(\text{reduction step}, 0\ V) + nqU \quad (12)$$

$$\Delta G(U) = \Delta G(\text{oxidation step}, 0\ V) - nqU \quad (13)$$

where n is the number of electron transferred. Additionally, the free energy of $H^+ + e^-$ are referenced to that of H_2 molecule using the standard hydrogen electrode ($\frac{1}{2} H_2 \leftrightarrow H^+ + e^-$,

ΔG =0 at U^{SHE} =0 V, pH=0, p = 1 atm, T = 298 K) which leads to the following expression:

$$\frac{1}{2}G_{H_2} = G(\mathrm{H}^+ + e^-) \quad (14)$$

This permits the use of gas phase values of H_2 in lieu of the energetics of solvated proton and electron pair in the liquid phase.

III. **A**

The atomically precise ligand protected gold clusters have emerged as hotly pursued class of nanoscale matter with potential applications as building blocks of nanostructured materials and devices as they show fascinating size-specific properties that are different from their bulk and traditional nanoparticle counterpart.[14-18]. Aside from tremendous advances achieved in understanding their structures and electronic properties, efforts were undertaken to address their potential catalytic properties. For example, the negatively charged thiolate-protected $Au_{25}(SR)_{18}^-$ cluster (denoted hereon as Au_{25}) has structure containing an icosahedral Au_{13} core with a protective gold thiolate layer of six RS-Au-RS-Au-RS oligomeric subunits.[19-21] In the protective subunit, the Au atoms are linked by bridging thiolate groups covalently linked to the core by sulfur in an approximately atop positions. It was detected to be markedly active for oxidation of styrene and cyclohexane, hydrogenation of aldehydes and ketones and electrochemical reduction of O_2.[22-24] Our group also reported the ability of this material to produce CO via electrochemical reduction of CO_2 in aqueous solution.[25] The product begins to form at an onset potential of -0.193 V *vs* the reversible hydrogen electrode (RHE) at ambient conditions. A current efficiency of nearly 100 % for CO formation was achieved at -1V *vs* RHE with

concomitant rate that is much higher compared to bulk Au catalysts. It was suggested from DFT calculations that the predicted stable adsorption of CO_2 on specific pocket sites on the intact cluster was the key step in the conversion process.

We subsequently revisited this process employing the CHE method with the objective of further characterizing the reaction mechanism.[26]. From an atomic-scale perspective, the CO_2 reduction reaction (CO_2RR) is suggested to proceed via two-electron pathway according to:[27, 28]

$$CO_{2(g)} + H^+_{(aq)} + e^- + * \rightarrow *COOH \quad \text{(I)}$$

$$*COOH + H^+_{(aq)} + e^- \rightarrow *CO + H_2O_{(aq)} \quad \text{(II)}$$

$$*CO \rightarrow CO_{(g)} + * \quad \text{(III)}$$

where * , *COOH and *CO represents a binding site, adsorbed COOH and adsorbed CO. In this reaction sequence, the binding strength of COOH and CO will be a key predictor to the performance. That is, the energetic stabilization and reduction of *COOH (steps I-II) dictates the ease of formation of CO.

The analysis was begun by looking at the CO_2RR on the fully ligand protected cluster and the result at 0 V vs RHE is shown in Fig. 1. The reaction onset potential is an important parameter that can be extracted from the calculated free energy diagrams and directly compared with experimental data. This is defined as the potential at which in the product direction, all reaction steps become downhill or exothermic in free energy, namely $U_{onset} = \max((\Delta G_I, \Delta G_{II}, \Delta G_{III})/e)$ where ΔG_i is the free energy for reaction step *i* at *U* = 0 V while *e* is the charge of an electron.[29] Thus, the onset potential is the minimum applied potential required to facilitate the formation of relevant intermediates. We see that the pathway on the intact cluster has a

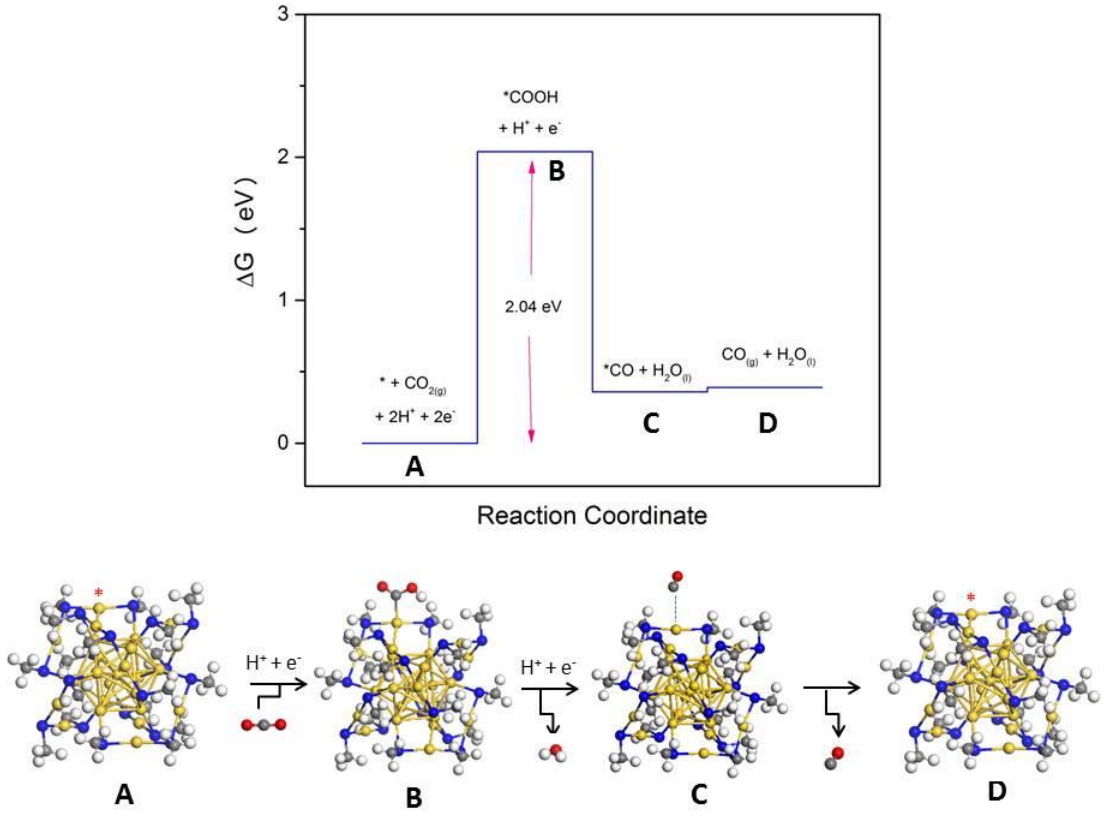

Fig. 1. Free energy diagram of for electrochemical reduction of CO_2 to CO on the intact cluster at T = 298 K, pH=0 and zero applied potential. White, gray, blue, gold and red balls represent H, C, S, Au atom and O atoms, respectively.

predicted onset potential of U_{onset} = -2.04 V with $CO_{2(g)} + H^+_{(aq)} + e^- + * \rightarrow$ *COOH as the corresponding potential determining step. This value is far larger than the experimentally determined value of -0.193 V. However, if we now consider the onset potential on a model defective cluster generated by removal of a single thiolate ligand exposing a gold atom, we see a dramatic difference (Fig. 2). The key outcome is that *COOH formation is dramatically stabilized on the dethiolated cluster compared with the intact one with corresponding U_{onset} = -0.34 V which is relatively much closer to the experimental value. The very high predicted U_{onset} suggests that CO_2 reduction on the

fully ligand protected species is ruled out unless very high potentials are applied. The most feasible pathway requires a condition in which at least a thiolate ligand is lost and a free gold atom is now exposed in the cluster.

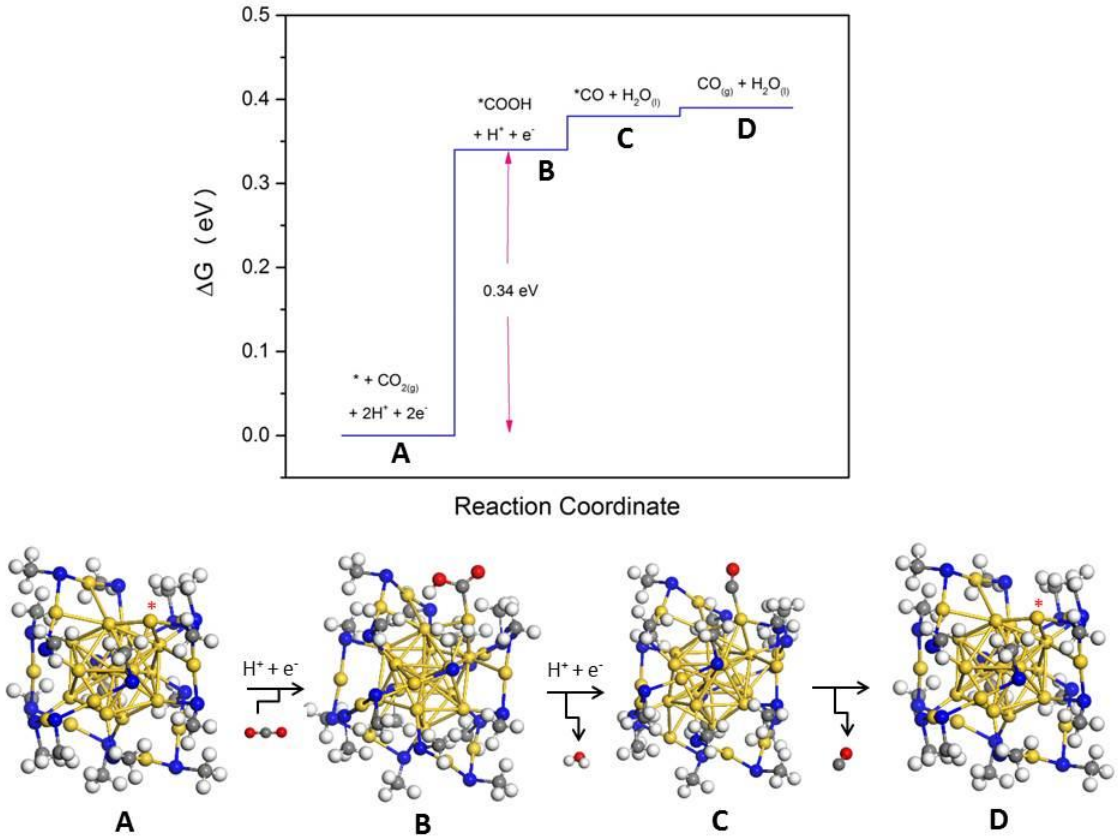

Fig. 2. Free energy diagram of for electrochemical reduction of CO_2 to CO on the dethiolated cluster at T = 298 K, pH=0 and zero applied potential. White, gray, blue, gold and red balls represent H, C, S, Au atom and O atoms, respectively

III.B

Reports of using metal nanoclusters as systems for providing platforms for CO_2 electrocatalytic conversion have begun to increase with Au, Cu and Pd as the metal components.[30-33] These structures maximize the area of catalytic active sites and also show size dependent catalytic properties. For example, Mistry *et al*. fabricated Au nanoparticles

with size ranging from 1.1-7.7 nm to ascertain their performance for CO_2 electroreduction. [31]With decreasing size, samples were found to exhibit jump in the in the overall catalytic activity at -1.2 V vs SHE with the hydrogen evolution process (HER) becoming more dominant for those below 5 nm. The concomitant DFT calculations suggest substantial stabilization of intermediates attributed to the decrease of coordination number of the active sites. Similar to Au, the decrease in the coordination number in Cu and Pd nanoparticles is linked to their significant change in the activity and product distribution. [32, 33]

We previously reported the use of CHE approach to further explore these phenomena. The CO_2RR on Au, Ag, Cu, Ir, Ni, Pd, Pt and Rh nanoparticles with different sizes were examined including the impact of the competing HER.[34] Model icosahedron metal nanoparticles between ~ 0.5 to ~2.0 nm diameter (particle size of 13, 55 and 309 atoms) were considered (Fig. 3). . For CO_2RR, steps I-III was adopted while the HER consisted of two consecutive proton-electron pair steps: [31, 35]

$$H^+_{(aq)} + e^- + * \rightarrow *H \quad \text{(IV)}$$

$$*H + H^+_{(aq)} + e^- \rightarrow * + H_2 \quad \text{(V)}$$

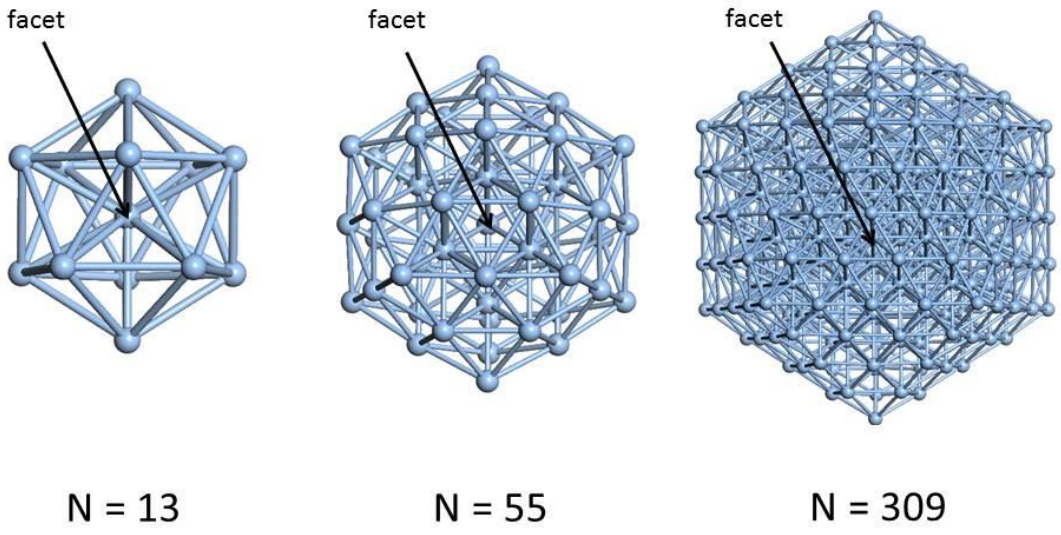

Figure 3. Schematic view of model icosahedron nanoparticles with different sizes showing the location of the "facet" active+ sites.

First, considering the CO_2RR on the coinage metals (Fig. 4a), we see that *COOH formation is limiting the reaction at 0 V for the 55 and 309 atom clusters with reduction in thermodynamic barrier as the size decreases. *COOH is generally more stabilized at Cu_{55} and Cu_{309}, and they are expected to more efficiently reduce CO_2 into COOH compared with Ag and Au. In all cases, stabilization of *COOH is accompanied by concomitant stabilization of *CO. Though *COOH formation remains the most difficult step on Cu_{55} and Cu_{309}, the production CO is predicted to be more difficult since the corresponding desorption event becomes more energetically unfavorable. In contrast, the most energetically difficult step for the smallest 13 atom cluster is the desorption or further

reduction of *CO and CO poisoning is a likely problem. In the case of HER, the $H^+ + e^- \rightarrow$ *H step becomes more favorable with decreasing particle size (Fig. 4b). On all Cu, it is favorable due to strong *H adsorption. The reduction step becomes spontaneous for the smallest cluster while the desorption step becomes uphill.

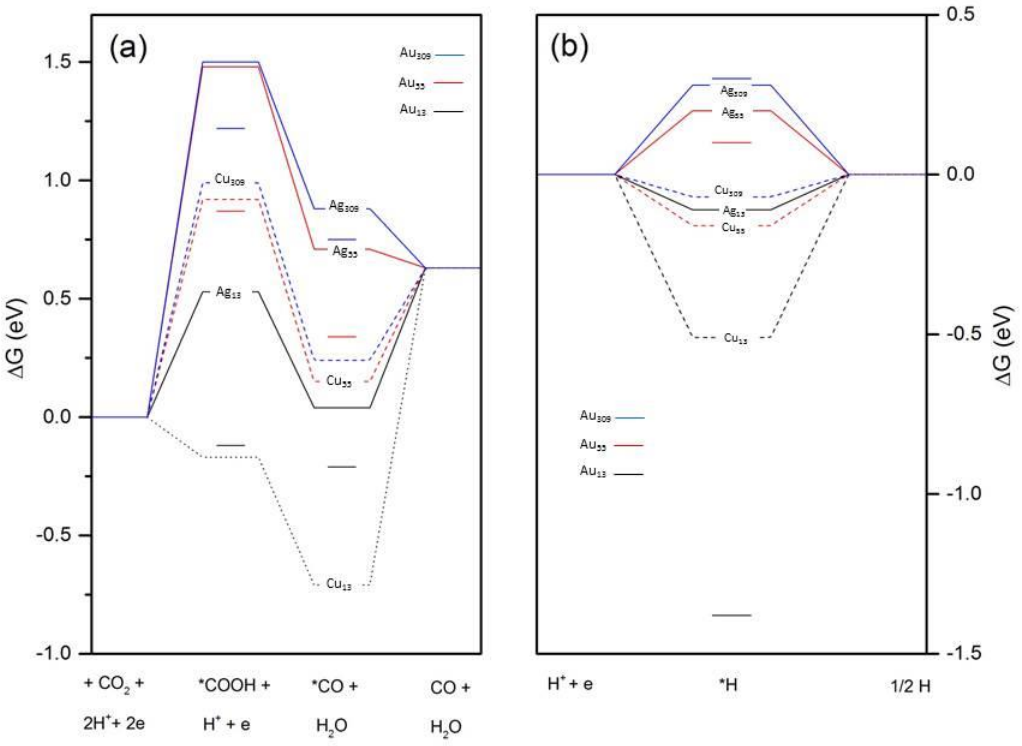

Figure 4. Free energy diagrams for (a) CO_2RR and (b) HER on Au, Ag and Cu NPs.

Having established the CO_2RR and HER for the coinage metals, we then looked at trends across the other metals. For a given size, the transition metals are predicted to bind COOH species more strongly than coinage metals, meaning that *COOH formation is a relatively favorable step on the transition metals, However, this is offset by stronger *CO binding affinity. Figure 5 shows the most difficult step in the CO_2RR pathway and the

associated free energy barriers at all NPs. These results predict the release of gaseous CO is sluggish for all transition metal NPs. For the coinage metals, only the 13-atom clusters exhibit this behavior. It should be noted that the other obstacle preventing efficient CO_2 reduction is the potential hydrogen poisoning of the active site. Comparison of the

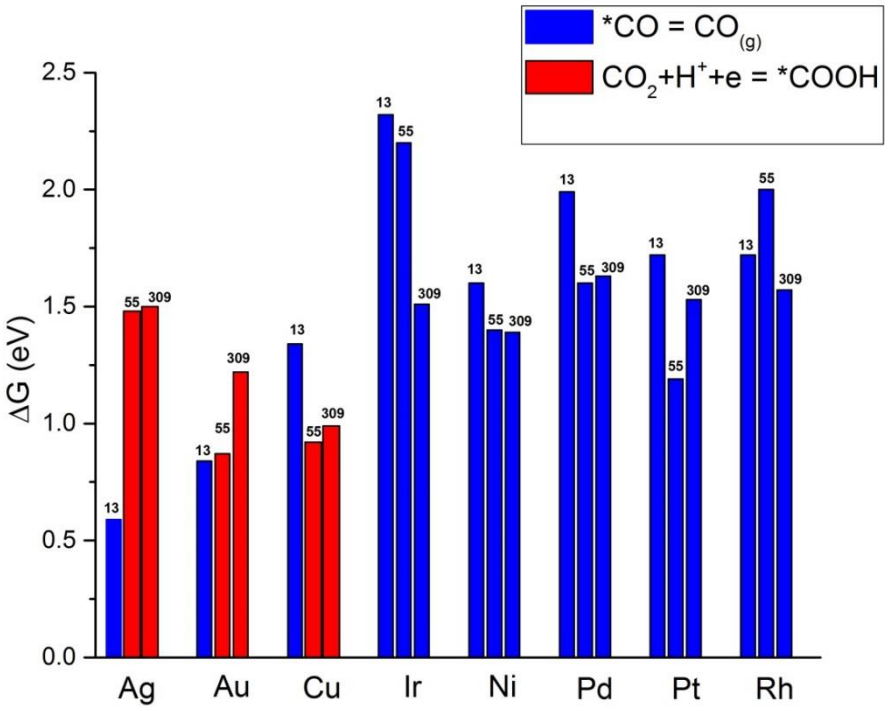

Figure 5. Calculated free energy barrier for the most difficult step in the reduction pathway for each metal. The blue and red bars correspond to *CO desorption and *COOH formation, respectively. For each metal, the left, center and right bars represent 13, 55 and 309 atom clusters.

ΔG for *H and *COOH formation at all NPs indicate that *H formation is more favorable. Thus, the calculations predict that all NPs will preferentially adsorbed hydrogen at cathodic potentials.

III. C

Organometallics complexes composed of earth-abundant metals have been reported to efficiently electrocatalyze hydrogen and oxygen evolution reactions.[36, 37 38] Unlike heterogeneous catalysts, the reactive surface structure of these small organometallics can be accurately described, and the active sites identified. In our group we recently synthesized and characterized small size metal thiolate complexes $M_6(SCH_3)_{12}$ with M = Fe, Pd, and Rh to electrocatalyze oxygen evolution reactions using computational techniques and thermodynamic analysis. [38] These stable complexes possess a tiara-like structure stabilized by metal-S π bonds, where the six metal atoms are distributed in a nearly hexagonal ring with twelve bridging sulfur atoms (see Figure 6). In these materials, the OER occurs at potentials that are more anodic than the transition metal oxidation wave. Therefore, the reactive surfaces are covered with 5/6 oxygen monolayer leaving one metal cation vacant as active site (Figure 6a).

It has been shown that the onset potential and corresponding potential determining steps can be extracted from OER free energy diagrams.[29, 39] Typically, OER involves four major steps and each step is accompanied with a release of a proton and electron. The reaction initiates from the oxidation of a water molecule with adsorption of OH* on the free metal site. The adsorbed OH* then oxidized into O* which reacts with another water molecule to form OOH*. After further oxidation, the OOH* intermediate is desorbed from the electrode, releasing O_2 gas as final product (Figure 6a-b). We predicted the onset potential of these complexes to increase as Ni < Rh < Pd < Fe. This increase was directly associated to the binding affinity of the transition metal with the intermediates. We noted that the adsorption strength of O, OH, and OOH follows the order Pd < Ni <

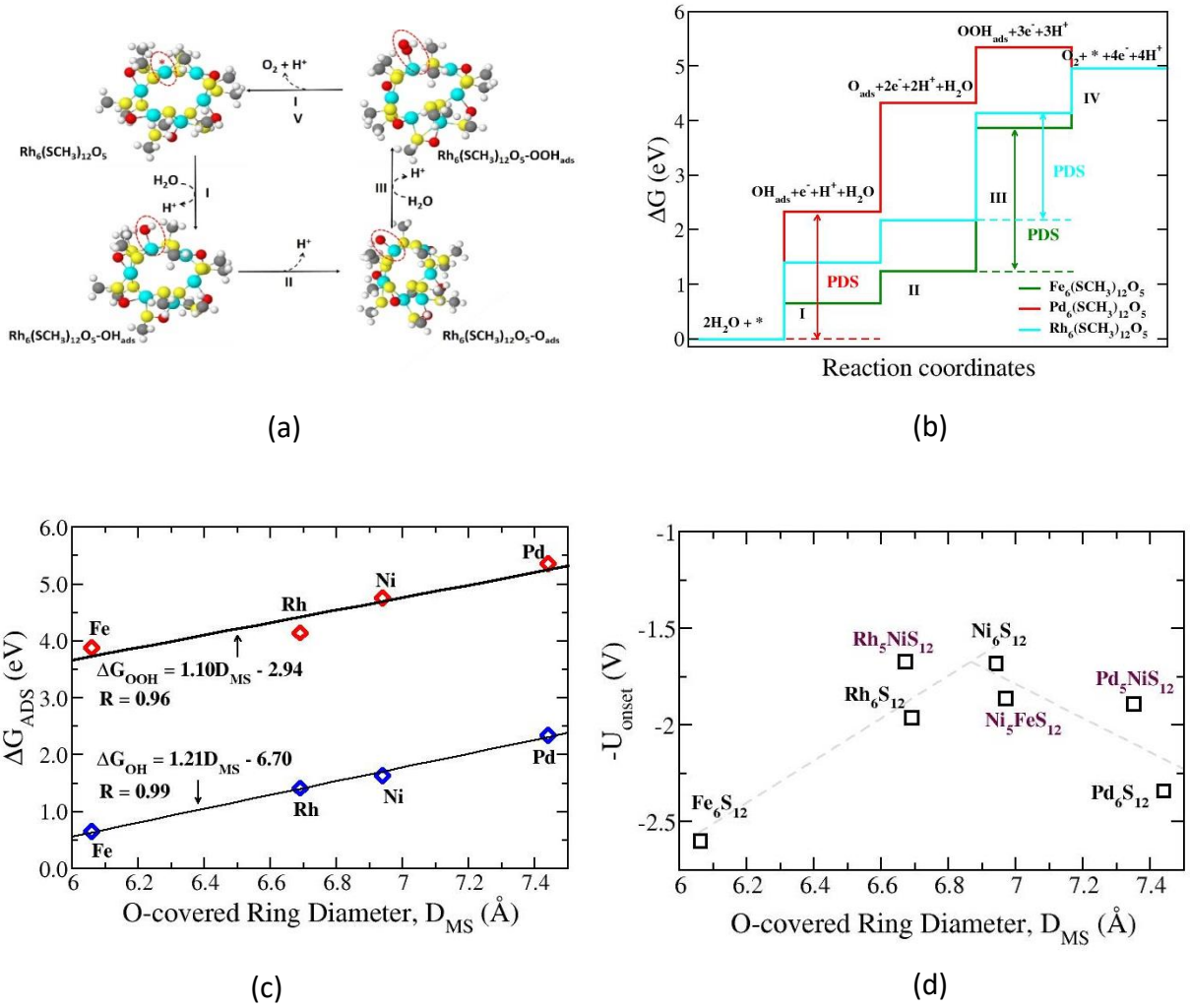

Figure 6. Schematic of the OER on $M_6(SCH_3)_{12}O_5$ (M = Fe, Pd, Rh) at room temperature and zero applied potential. (a) Predicted structures for all intermediates on $Rh_6(SCH_3)_{12}O_5$. The adsorbed OER intermediates are highlighted with red dashed circle; (b) Gibbs free energy of reactions; (c) Trends in ΔG_{OH} and ΔG_{OOH} described by the diameter of the O-covered M_6S_{12} ring, D_{MS}. Least-squares fits are provided together with the correlation coefficients. (d) Plot of the onset potential, U_{onset}, versus the diameter of the O-covered M_6S_{12} (M = Fe, Rh, Ni, Pd) ring. Also included are the doped complexes (maroon color). The dashed lines are to guide the eyes. Adapted and reprinted with permission from Ref. [38] Copyright (2018) Elsevier B. V.

Rh < Fe, with the strongest adsorption on Fe which results to a larger overpotential (Figure 6c). We also observed that these adsorption strengths (energies) correlated linearly with the ring diameter of the oxidized complexes. Moreover, the predicted

overpotential showed a maximum activity at Ni complex when plotted against the diameter of the hexagonal ring, suggesting that the ring diameter of the oxidized complexes can be used as descriptors for OER activity (Figure 6d). [38]

To improve OER activity, surface modification through doping/substitution has proven to be an efficient strategy. For example, Liao and co-workers increase the OER activity of hematite by doping it with Ni and Co.[40] Garcia-Mota and co-workers tailored the activity for OER on rutile TiO_2 surface by transition-metal substitution and found a lower overpotential for the doped-TiO_2.[41] We modified the surface of these organometallics by substituting the metal active site in $M_6(SCH_3)_{12}$ (M = Rh, Pd, Fe) with a Ni atom. We found a reduction of the onset potential by approximately 0.45 and 0.29 V for Pd and Rh complexes, respectively. Detailed analysis revealed that the enhanced overpotential is caused by a shift of the binding energies of intermediates with Ni active sites surrounded by Pd or Rh toward that of $Ni_6(SCH_3)O_5$.

III. Beyond the computational hydrogen electrode method: The Grand Canonical Density Functional Theory Approach

Any method that aims to improve over the CHE method has to take into account the full details of the influence of the interaction between species and the electrode itself at a specific potential. Efforts have been made by Filhol and Neurock to go beyond the thermodynamic approximation by adding and removing fractions of electrons coupled with the inclusion of a uniform background countercharge.[42] In the approach of Ottani and Sugino, external potential is included by dragging electrons from one side of the periodic slab to another.[43] The scheme of Skulason *et al* involves varying proton/electron concentration to study a system as a function of electrode potential.[44] While these

schemes are conceptually simple, the computational expense can be immense especially for modeling larger systems such as nanoparticles.

In recent years, advances have been accomplished in the implementation of constant potential schemes within the framework of quantum mechanical approaches. In particular, Sundararaman *et al* presented a scheme for carrying out constant chemical potential μ calculations based on finite temperature grand canonical DFT ansatz where the number of electrons *N* adjusts accordingly as dependent variables.[9] The relevant free energy minimized at equilibrium is the grand free energy:

$$\Omega = A - \mu N$$

where *A* is defined as:

$$A = A_{JDFT}[n(\vec{r}), N_\alpha(\vec{r})] + \int d\vec{r} V(\vec{r}) n(\vec{r}) + \sum_\alpha \int d\vec{r} V_a(\vec{r})$$

The last two terms represent effects due to external electron potential and the external potential on the liquid nuclei. The first term A_{JDFT} is a universal functional independent of these external potentials expressed as a sum of Hohenberg-Kohn electronic density functional for the solute and a solvation term in which the liquid is described directly in terms of its average density rather than individual configurations. Therefore, this model combines solvent treatment and explicit accounting of the electrochemical potential. Another crucial point is the convergence of the overall scheme. The conventional route is to converge the energy given an initial number of electrons. The number of electrons is then changed by ΔN to obtain a new value for μ. This procedure is carried out until a converged wave function is obtained at the desired value of the chemical potential. The disadvantage of this approach is that the number of iterations needed can be fairly high resulting into considerable computational overhead. Direct minimization of the free

energy functional Ω with respect to the Kohn-Sham orbitals represents an attempt to simultaneously achieve computational efficiency and accuracy. Briefly, the algorithm employs a robust analytically continued functional for energy minimization instead of the typical self-consistent field schemes. The readers are referred to Ref.[9] for further details.

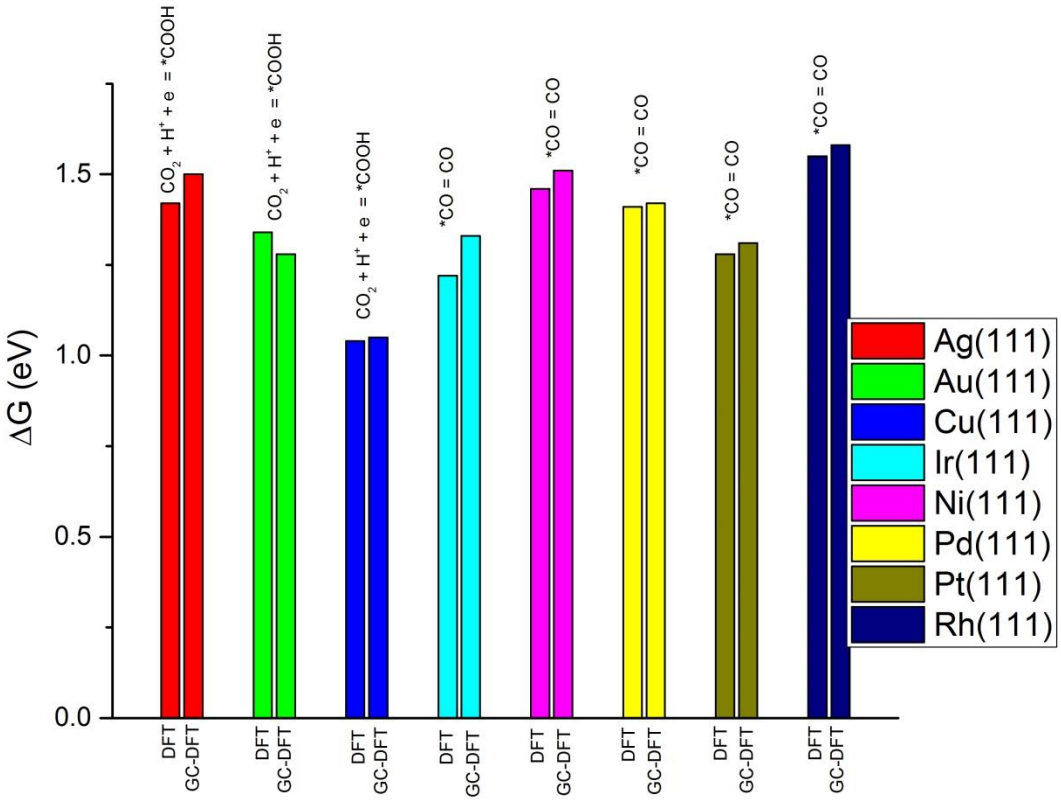

.

IV. CONCLUSION

In summary, we theoretically examined the mechanistic, thermodynamic and kinetic aspects of the CO + NO chemistry on Rh(111). We considered the scenario that the reaction step leading to the formation of N_2 occurs through the conventional *N + *N recombination step and via formation of $*N_2O$ intermediary species. Our initial DFT analysis reveals that the one that proceeds through the association of *NO and *N may be an important pathway not only for N_2 formation but for N_2O as well. Quantities computed using DFT were incorporated into a microkinetic model to elucidate the NO reduction by CO as a function of temperature for typical sets of combustion exhaust condition. The level of agreement between our predictions and experiments allow us to obtain useful trends relevant to NO + CO chemistry on Rh(111). Our simulation shows that N_2O is a major product in addition to N_2 and CO_2. The presence of high simultaneous coverage of *NO and N* promotes N_2O formation. This situation also makes the $*N + *NO \rightarrow *N_2O \rightarrow *N_2 + *O$ pathway an important contributor to N_2 formation in addition to classical *N + *N step.

ACKNOWLEDGMENTS

This report was prepared as an account of work sponsored by an agency of the United States Government. Neither the United States Government nor any agency thereof, nor any of their employees, makes any warranty, express or implied, or assumes any legal liability or responsibility for the accuracy, completeness, or usefulness of any information, apparatus, product, or process disclosed, or represents that its use would not infringe privately owned rights. Reference herein to any specific commercial product, process, or service by trade name, trademark, manufacturer, or otherwise does not necessarily constitute or imply its endorsement, recommendation, or favoring by the United States Government or any agency thereof. The views and opinions of author(s) expressed herein do not necessarily state or reflect those of the United States Government or any agency thereof.

REFERENCES

[1] M. Gattrell, N. Gupta and A. Co, J. Electochem. Chem. **594**, 1 (2006).
[2] Y. Hori, *Modern Aspects of Electrochemistry*. (Springer, New York, 2008).
[3] M. Aresta, *Carbon Dioxide as Chemical Feedstock*. (Wiley, Wienheim, 2010).
[4] I. Ganesh, Renewable Sustainable Energy Rev. **31**, 221 (2014).
[5] F. Calle-Vallejo and M. T. M. Koper, Electrochim. Acta **84**, 3 (2012).
[6] S. N. Steinmann, C. Michel, R. Schwiedernoch and P. Sautet, Phys. Chem. Chem. Phys. **17**, 13949 (2015).
[7] J. Hafner, J. Comput. Chem. **29**, 2044 (2008).
[8] K. Letchworth-Weaver and A. T. Arias, Phys, Rev, B **86**, 075140 (2012).
[9] R. Sundararaman, W. A. Goddard and A. T. Arias, J. Chem. Phys. **146**, 114104 (2017).
[10] J. K. Norskov, J. Rossmeisl, A. Logadottir, L. Linqvist, J. R. Kitchin, T. Bligaard and H. Jonnson, J. Phys. Chem. B **108**, 17886-17892 (2004).
[11] K. E. Gubbins and J. D. Moore, Ind. Eng. Chem. Res. **49**, 3026 (2010).
[12] K. Matthew, R. Sundararaman, K. Lechtworth-Weaver, T. A. Arias and R. Hennig, J. Chem. Phys. **140**, 084106 (2014).
[13] V. K. Shen, D. W. Siderius, W. P. Krekelberg and H. W. Hatch, (National Institute of Standards and Technology, Gaithersburg MD, 20899).
[14] M. C. Daniel and D. Astruc Chem. Rev. **103**, 293 (2004).
[15] R. Sardar, A. M. Funston, P. Mulvaney and R. Murray, Langmuir **25**, 13480 (2009).
[16] P. Rodriguez, Y. Kwon and M. T. M. Koper, Nature Chem. **4**, 177 (2012).

[17] R. Jin, Nanoscale **2**, 343 (2010).
[18] J. F. Parker, C. A. Fields-Zinna and R. W. Murray, Acc. Chem. Res. **43**, 1289 (2010).
[19] M. W. Heaven, A. Dass, P. S. White, H. K. M. and R. W. Murray, J. Am. Chem. Soc. **130**, 3754-3755 (2008).
[20] M. Zhu, C. M. Aikens, F. J. Hollander, G. C. Schatz and R. Jin, J. Am. Chem. Soc. **130**, 5883-5885 (2008).
[21] J. Akola, M. Walter, R. L. Whetten, H. Hakkinen and H. Gronbeck, J. Am. Chem. Soc. **130**, 3756-3757 (2008).
[22] Y. Zhu, H. Qian and R. Jin, J. Mater. Chem. **21**, 6793 (2011).
[23] Y. Zhu, H. Qian, B. A. Drake and R. Jin, Angew. Chem. Int. Ed. **59**, 1295 (2010).
[24] W. Chen and S. Chen, Angew. Chem. Int. Ed. **48**, 4386 (2009).
[25] D. Kauffman, D. Alfonso, C. Matranga, H. Qian and R. Jin, J. Am. Chem. Soc. **134**, 10237-10243 (2012).
[26] D. Alfonso, D. Kauffman and C. Matranga, J. Chem. Phys. **144**, 184705 (2016).
[27] A. A. Peterson, F. Abild-Pedersen, F. Studt, J. Rossmeisl and J. K. Norskov, Energy Environ. Sci. **3**, 1311-1315 (2010).
[28] H. A. Hansen, J. B. Varley, A. A. Peterson and J. Norskov, J. Phys. Chem. Lett. **4**, 388 (2013).
[29] J. Rossmeisl, Z. W. Qu, H. Zhu, G. J. Kroes and J. K. Norskov, J. ElectroAnal. Chem **607**, 83 (2007).
[30] W. Zhu, R. Michalski, M. O., H. Lv, S. Guo, C. J. Wright, X. Sun, A. A. Peterson and S. Sun, J. Am. Chem. Soc. **135**, 16833-16836 (2013).
[31] H. Mistry, R. Reske, Z. Zeng, Z.-J. Zhao, J. Greeley, P. Strasser and B. Roldan Cuenya, J. Am. Chem. Soc. **136**, 16473-16476 (2014).
[32] R. Reske, H. Mistry, F. Behafarid, B. Cuenya and P. Strasser, J. Am. Chem. Soc. **136**, 6978 (2014).
[33] D. Gao, H. Zhou, J. Wang, S. Miao, F. Yang, G. Wang, J. Wang and X. Bao, J. Am. Chem. Soc. **137**, 4288 (2015).
[34] D. Alfonso and D. Kauffman, MRS Communication **7**, 601 (2017).
[35] W. Zhu, W. J. Zhang, H. Zhang, H. Lv, Q. Li, R. Michalski, A. A. Peterson and S. Sun, J. Am. Chem. Soc. **136**, 16132-16135 (2014).
[36] M. L. Helm, M. P. Stewart, R. M. Bullock, M. R. Dubois and D. L. Dubois, Science **333**, 863 (2011).
[37] D. Kauffman, D. Alfonso, D. Tafen, J. Lekse, C. Wang, X. Deng, J. Lee, H. Jang, J.-s. Lee, S. Kumar and C. Matranga, ACS Catal. **6**, 1225 (2016).
[38] D. Tafen, D. Kauffman and D. Alfonso, Comp. Mat. Sci **150**, 283 (2018).
[39] M. Bajdich, M. Garcia-Mota, A. Vojvodic, J. Norskov and A. T. Bell, J. Am. Chem. Soc. **135**, 13521 (2013).
[40] P. Liao, J. A. Keith and E. A. Carter, J. Am. Chem. Soc. **134**, 13296 (2012).
[41] M. Garcia-Mota, A. Vojvodic, H. Metiu, I. C. Man, H. Y. Su, J. Rossmeisl and J. Norskov, ChemCatChem **3**, 1607 (2011).
[42] J. S. Filhol and M. Neurock, Angew. Chem. Int. Ed. **45**, 402 (2006).
[43] M. Otani and O. Sugino, Phys, Rev, B **73**, 115407 (2006).
[44] E. Skulason, V. Tripkovic, M. E. Bjorketum, S. Gudmunsdottir, G. Karlberg, J. Rossmeisl, T. Bligaard, H. Jonsson and J. Norskov, J. Phys. Chem. C **114**, 18182-18197 (2010).